



Fast reactions with nano- and micrometer aluminum: A study on oxidation versus fluorination

Kyle W. Watson, Michelle L. Pantoya*, Valery I. Levitas¹

Department of Mechanical Engineering, Texas Tech University, Lubbock, TX 79409, USA

Received 21 January 2008; received in revised form 27 May 2008; accepted 3 June 2008

Available online 28 July 2008

Abstract

The use of fluorine as an oxidizing agent in aluminum (Al)-based thermite reactions yields higher peak pressures and an increase in gas production compared with oxygen-containing oxidizers, such as molybdenum trioxide (MoO_3). Thus fluorination reactions have the potential to excel in situations that require high pressures and flame speeds. This study compares the combustion behaviors of Al/Teflon, Al/ MoO_3 /Teflon, and Al/ MoO_3 in an effort to determine the effects that the replacement of oxygen with fluorine has on the reaction dynamics in both open and confined burning configurations. Data were collected from pressure sensors and high-speed imaging. The mass percent of Al was varied from 10 to 90% to study the effects of composition. The composites were then further tested at the optimum stoichiometry using either 50 nm or 1–3 μm Al to examine the effect of Al particle size. The addition of Teflon in an open configuration hinders the reaction due to a loss of liberated gas. Confining the reaction enables the trapped gases to enhance convection, yielding increased flame speeds. For confined conditions, the reactions containing Teflon exhibit higher peak pressures but lower flame speeds than the reactions with MoO_3 . These results imply that a direct relationship between generated gas pressures and flame speeds does not generally exist when comparing different oxidizers. The theoretically predicted relationship for the relative flame speed versus relative particle size based on the melt-dispersion mechanism agrees with experimental data for all Al particle sizes and for the fluorination reaction. Particle synthesis parameters are suggested that could be controlled to enable micrometer-scale Al particles to achieve the performance of nanoscale Al particles. This is of significant practical importance, because nanoparticles are 30 to 50 times more expensive than the micrometer particles.

© 2008 The Combustion Institute. Published by Elsevier Inc. All rights reserved.

Keywords: Aluminum particle combustion; Fluorination; Thermites; Flame speeds; Reaction mechanisms; Melt-dispersion mechanism

1. Introduction

The introduction of nanoscale particles into energetic materials, specifically thermites, has provided the means to tailor parameters such as sensitivity, stability, gas generation, and energy release [1,2]. The traditional thermite reaction is defined as “an exothermic reaction which involves a metal reacting with a

* Corresponding author. Fax: +1 806 742 3540.

E-mail address: michelle.pantoya@ttu.edu
(M.L. Pantoya).

URL: <http://www.depts.ttu.edu/combustionlab/>

¹ Present address: Iowa State University, Departments of Mechanical Engineering, Aerospace Engineering, and Material Science and Engineering, Ames, IA 50011, USA.

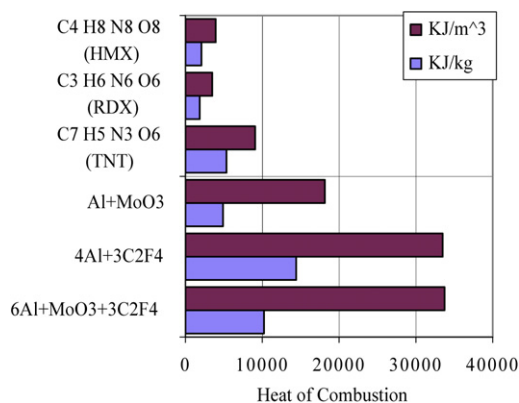


Fig. 1. Heat of combustion for various compositions determined from REAL Code (Tim Tec, LLC) calculations, a chemical equilibrium program tailored for energetic materials.

metallic or a non-metallic oxide to form a more stable oxide and the corresponding metal or non-metal of the reactant oxide” [3]. A new class of thermites referred to as metastable intermolecular composites (MIC) has been described as “mixtures of nanoscale powders of reactants that exhibit thermite (high exothermicity) behavior” [2]. This new class of composites utilizes nanoscale powders that result in much higher propagation rates and ignition sensitivity than their micrometer-scale counterparts [4–6].

One particularly interesting MIC is the aluminum (Al) and Teflon composite because the fluorine from Teflon replaces oxygen from the metal oxide as the oxidizer. Fluorine is the most electronegative element making it an excellent candidate as an oxidizer in a reduction–oxidation reaction. It has the potential to exceed oxygen’s reactive power as illustrated in Fig. 1. Teflon, or polytetrafluoroethylene, is a prime candidate as a fluorine source for use in fluorination reactions. Manufactured by Dupont under the name Teflon, polytetrafluoroethylene is composed of a C_2F_4 molecular structure and has a 75 wt% of fluorine. The reaction of Al with Teflon generates 21 GJ/m^3 (Fig. 1), compared with the best molecular explosive that generates less than 12 GJ/m^3 [7]. Kubota and Serizawa [8] found that magnesium (Mg) with fluorine produces a heat of combustion of 16.8 MJ/kg of Mg which is higher than the heat of combustion produced by magnesium with oxygen (13.8 MJ/kg). Lips [9] showed that using highly fluorinated oxidizers, in the form of liquid fluorine–oxygen mixtures, in combination with highly aluminumized rocket fuels, resulted in more efficient combustion of aluminum particles than reactions that contained no fluorine. The highly fluorinated reactions also exhibited an increase in regression rate and maintained the performance of nonfluorinated reactions [9].

As Al particle size decreases there is a decrease in its melting enthalpy and melting temperature [10–12]. The melting temperature depression is theorized to be an effect of the increased fraction of surface atoms with decreased particle size [10,11]. As the particle size decreases the surface to volume ratio increases dramatically (i.e., on the order of $1/\text{radius}$). When mixed as a composite this increase allows for an increase in the number of contact points with the oxidizer and improved mixture homogeneity [13]. Also, on the nanoscale, the mechanism by which a reaction can occur will shift from diffusion to melt-dispersion-controlled process [14,15].

For the fluorine in Teflon to be available for reaction with a fuel, Teflon must first be degraded. The thermal decomposition of Teflon is the reverse reaction of its polymerization. It requires an energy input equal to the heat released during its formation, which is approximately 172 kJ/kg [16,17]. Teflon melts at 595 K and decomposes starting around 803 K and completing around 893 K [18]. During this decomposition an exothermic gasification reaction occurs and fluorine is abundantly produced [18–20].

Osborne and Pantoya [20] showed via differential scanning calorimetry (DSC) and thermogravimetric analysis (TGA) that much of fluorine in micrometer-scale Al/Teflon escaped the reaction zone before reacting with the micrometer Al particles when subjected to slow heating conditions. Osborne and Pantoya [20] found that the mixture lost $\sim 25\%$ of its mass before the reaction with Al occurred meaning that only $\sim 17\%$ of the Teflon reacted with the Al. They also found that this did not occur when the same experiments were conducted using nanoscale Al in the Al/Teflon composites. The nano-Al mixture only lost $\sim 6\%$ of its mass before the reaction with Al implying that 75% of the Teflon reacted with Al. This may be attributed to the increased ignition sensitivity associated with nano-Al particles which were able to react with the fluorine oxidizer before it escaped. Results by Osborne and Pantoya [20] suggest that the Al/Teflon composites utilizing micrometer Al particles may lose much fluorine oxidizer to the atmosphere prior to Al ignition and reaction.

Dolgovorodov et al. [21] studied Teflon-based mechanoactivated energetic composites such as Al-Teflon. With spherical Al particles of $4 \mu\text{m}$ in diameter, they measured burning velocities between 300 and 400 m/s . The Al/Teflon reactions have the potential to show increased flame speeds based on the increased amount of product gases, higher heats of reaction (Fig. 1), and high flame speeds [21]. Also by confining micrometer Al/Teflon reactions, the fluorine is no longer able to escape and may exhibit a more complete reaction and faster propagation speed. One objective of this study is to examine the influ-

Table 1
Material properties of the reactants

Material	Particle diameter, D	Surface area	Morphology	Purity (%)	M	δ (nm)	R (nm)
Al	1–3 μm	<1 $\text{m}^2/\text{g}^{\text{a}}$	Spherical	99	438 ^a	1.1–3.4 ^a	498.9–1486.6
Al ^b	1–3 μm	N/A	N/A	98.6 ^a	312 ^a	1.6–4.8 ^a	498.4–1485.2
Al	50 nm	39.8 m^2/g	Spherical	75	14.2 ^a	1.6 ^a	23.4
Zonyl MP1150	200 nm	5–10 m^2/g	Spherical	99–100	N/A	N/A	N/A
MoO ₃	N/A	>50 $\text{m}^2/\text{g}^{\text{a}}$	Rectangular	99	N/A	N/A	N/A

^a Estimated values.

^b Does not correspond to actual material; small deviation from the Al content given by manufacturer is assumed for theoretical analysis.

ence of Teflon in the Al/Teflon and Al/MoO₃/Teflon reactions for loose powder mixtures burning in a confined apparatus compared with an open configuration. These reactions were also compared to the Al/MoO₃ reactions in order to better resolve the role of Teflon as a reducing agent in the reaction. This study will also examine the role of fuel particle size on the reaction behaviors by examining both nano- and micrometer-scale Al particles while the Teflon and MoO₃ particles are consistent nano-scale particles. Experiments were performed using photographic data to resolve flame speeds and piezoelectric pressure transducers to measure transient pressure behaviors.

Another goal of this study is to show experimentally that predictions based on the melt-dispersion mechanism (MDM) for 1- to 3- μm diameter Al particles can be applied to fluorination and theoretically predict how micrometer Al particles can achieve the performance of nanoparticles. This is of significant practical importance, because nanoparticles are 30 to 50 times more expensive than the micrometer-scale particles and they have safety and environmental issues which the micrometer particles do not have. It will be shown that experimental data are consistent with the melt-dispersion mechanism of oxidation for Al nanoparticles and that this theory can be generalized and applicable to fluorination reactions and for 1- to 3- μm diameter Al particles. Based on this theory, particle synthesis parameters are suggested that could be controlled to enable micrometer-scale Al particles to achieve the performance of nanoscale Al particles.

2. Experimental

Sample powders of Teflon (Dupont Zonyl MP-1150) and/or MoO₃ were combined with either 50 nm (NovaCentrix) or 1–3 μm Al (AEE) powder. The material properties are provided in Table 1. Note that the theoretical portion of this study included analysis of Al particles with deviations in material properties from those actually used in the experiments. For

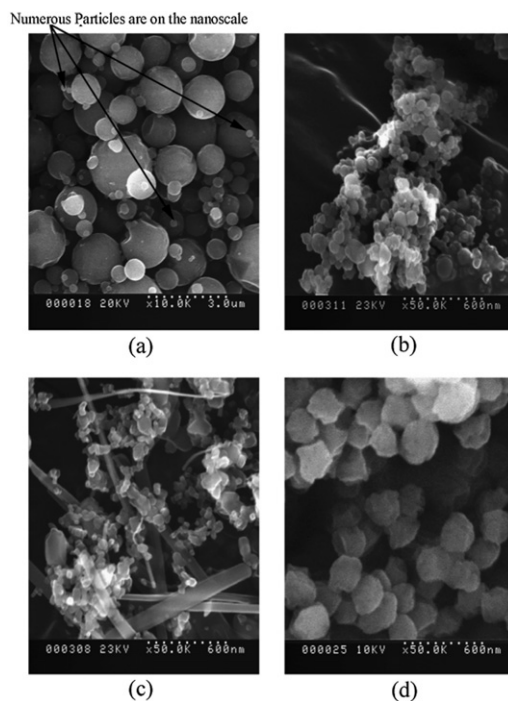


Fig. 2. SEM micrographs of the powders used prior to mixing: (a) 1–3 μm Al at 10,000 \times magnification; (b) 50 nm Al at 50,000 \times magnification; (c) rectangular MoO₃ at 50,000 \times magnification; (d) 200 nm Zonyl MP-1150 (Teflon).

this reason, data for the Al⁺ entry corresponds to an idealized Al particle considered theoretically but not actually used in experiments.

NovaCentrix Inc. (formerly Nanotechnologies, Austin, TX) uses X-ray diffraction, TEM imaging, and BET surface area analysis to verify particle size ranges and purity (i.e., active Al content) in a particle for the 50 nm Al. Dupont (Zonyl) and AEE (1–3 μm Al) use laser microtrac systems to determine particle size ranges. Scanning electron microscopy (SEM) images of the materials are provided in Fig. 2 to illustrate the extent in particle size range and amount of agglomeration in the premixed state. The micrometer-

scale Al powder appears to have a broad particle size distribution and contained particles that are on the nanoscale (Fig. 2).

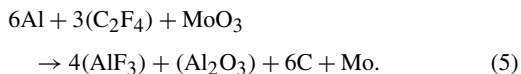
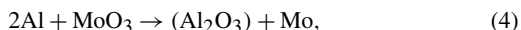
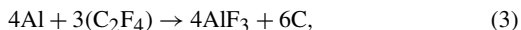
An important geometric parameter of the Al particle is the relative radius, M , which determines thermal stress development and fracture of the oxide shell and will be used in the theoretical analysis of the melt-dispersion mechanism applied to these reactions. Parameter M is the ratio of the Al core radius, R , to the oxide shell thickness, δ , i.e., $M = R/\delta$, and can be determined from the following mass balance in equations:

$$M = \frac{1}{Q - 1}, \quad (1)$$

$$Q = \left[\frac{\rho_{\text{Al}} + C(\rho_{\text{Al}_2\text{O}_3} - \rho_{\text{Al}})}{\rho_{\text{Al}_2\text{O}_3} C} \right]^{1/3}. \quad (2)$$

In Eq. (2), C is the active Al content in a particle and ρ is the mass density: $\rho_{\text{Al}_2\text{O}_3} = 3970 \text{ kg/m}^3$ and $\rho_{\text{Al}} = 2700 \text{ kg/m}^3$. Then, from the conditions $M = \frac{D}{2\delta} - 1$ and $R = M\delta$, parameters δ and R can be determined. Parameters R , δ , and M are given in Table 1 for nano- and micrometer particles. We will also theoretically consider small deviation from the Al content given by manufacturer, e.g., $C = 0.986$.

The powders were mixed by mass percent of pure Al ranging from 10 to 90%. The oxidizer consisted of 100% Teflon, 100% MoO_3 , or a mass ratio of 60% MoO_3 , and 40% Teflon. The following represent the stoichiometric reactions for these mixtures:



Mixing the composites over the 10 to 90% mass Al range resulted in large variations of equivalence ratios. Each composite is thus tested over a significantly different equivalence ratio range (i.e., 0.23–18.77 for Al/Teflon, 0.23–18.51 for Al/ MoO_3 /Teflon, 0.30–24.00 Al/ MoO_3). For this reason, the composites were compared by the mass percent of Al in the mixture rather than equivalence ratio.

Details on the mixing procedure can be found elsewhere [4–6]. In summary, the appropriate amount of powder for the desired composition is suspended in hexanes and subjected to ultrasonic waves using a Misonix Sonicator 3000 which breaks up agglomerates and promotes improved mixture homogeneity. The solution was then transferred to a glass pan and placed on a hotplate at 50°C for 10 min to allow evaporation of the liquid. The powder mixture was then reclaimed for use in the experiments. Fig. 3 displays the SEM images of the mixed powders that help

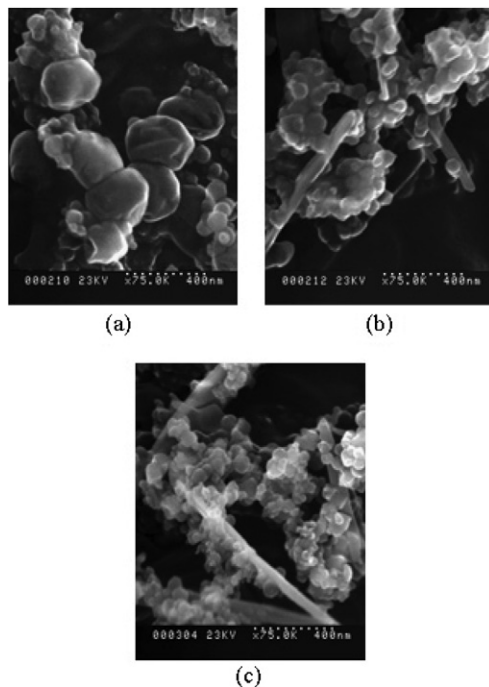


Fig. 3. SEM micrographs of the postmixed composites: (a) 50 nm Al/Teflon; (b) 50 nm Al/ MoO_3 ; (c) 50 nm Al/ MoO_3 /Teflon. All images taken at $75,000\times$ magnification.

visualize the homogeneity obtained from the mixing procedure.

The bulk density of the reactants will be described in terms of the theoretical maximum density (TMD). The TMD is calculated as the ratio of the actual mass of reactants divided by sample volume to the weighted average of pure solid densities of each reactant in the matrix. In this way, a TMD of 10% describes a sample that consists of 10% solid particles and 90% air voids.

2.1. Open burn setup

The open burn experiments consisted of the combustion of evenly distributed lines of loose powder composites. The loose powder was loaded evenly into a channel milled into an acrylic block. The block is of dimensions $152 \times 30 \times 12 \text{ mm}$, and the channel is of dimensions $107.95 \times 3.175 \times 2.54 \text{ mm}$ as pictured in Fig. 4A. Nichrome wire was secured at one end of the channel to provide an ignition source.

The testing was conducted in an inert argon chamber to eliminate any interaction of Al with ambient air. The argon chamber was fitted with acrylic viewing windows to allow the reaction to be recorded with a high-speed camera and pressure taps for pressure sensors.

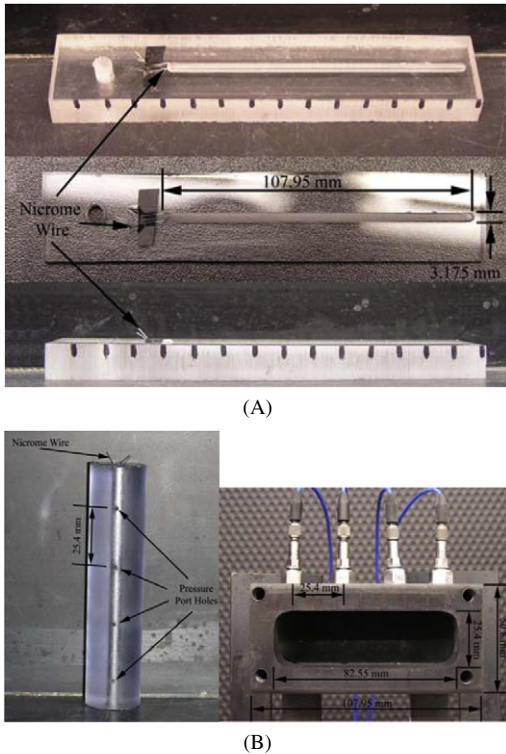


Fig. 4. (A) Photograph of open burn apparatus. Each interval corresponds to 1-cm increments used for defining a length scale for flame speed calculations. (B) Pictures of prepared burn tube and instrumented confined burn chamber. Note experiments were performed for tubes in horizontal direction.

2.2. Confined burn setup

The confined burn experiments consisted of confining loose powder composites in an instrumented tube similar to that originally designed by Bockmon et al. [6]. Polycarbonate tubes of 3.175 mm inner diameter, 25.4 mm outer diameter, and 107.95 mm length were used. The polycarbonate was chosen due to its high strength and optical clarity for viewing of the reaction. A nichrome wire was secured into one end of the tube for use as an ignition source. Fig. 4B illustrates this setup. The powder was loaded into the tube maintaining constant mass at each composition. The sample mass varied with changes in composition due to the change in density associated with different compositions. The tubes were lightly tapped to reduce voids and minimize density gradients without mechanically packing the powder. The tube was inserted into a 25.4-mm diameter opening bored through the center of a 50.8-mm-square by 108.0-mm long steel testing block instrumented with 4 PCB Model 113A22 pressure transducers at 25.4-mm increments. The testing block also had an 82.6×25.4 mm viewing window to allow data col-

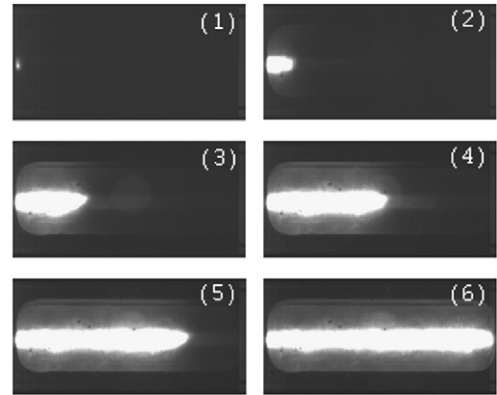


Fig. 5. Consecutive images displaying a typical confined burn. Each image corresponds to one frame at a sample rate of 40,000 fps. The front edge of luminous activity is used to calculate flame speed.

lection by the high-speed camera. The polycarbonate tube has small (<1 mm) holes that align with the pressure sensors. These holes provide ports for the pressure to escape and contact the pressure sensors.

The experiments were also conducted in the argon chamber to eliminate any possible reaction with the ambient air. Data collection was triggered manually and there was no synchronization between the data acquisition and the application of voltage to the Nichrome wire. Thus ignition sensitivity data were not collected and alterations in ignition sensitivity were not observed. Data were recorded in the form of flame propagation speed from the high-speed camera and pressure histories from the pressure sensors.

2.3. Data acquisition

Images from a Vision Research Phantom vs 7.1 high-speed camera were used to measure flame speed. The open burn experiments were recorded at 20,000 frames per second (fps). Confined burn experiments were recorded at 40,000 fps. The Phantom software calculates flame speed given a user defined length scale and a time scale dependent on the sample rate of recording. The software tracks the displacement of the flame front, considered here as the front edge of luminous activity. A series of consecutive frames shows the progression of the flame front in the confined state in Fig. 5.

The pressure transducers were used to measure pressures generated in the confined burns. The PCB Model 113A22 transducers are routed to a PCB Model 482A22 signal conditioner and subsequently to a National Instruments BNC-2110 data acquisition board. The National Instruments board was controlled using Labview version 8.0. Sample rates for tests with micrometer-scaled AI were 50,000 points per second

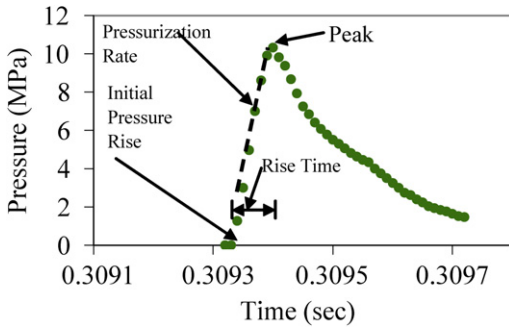


Fig. 6. Typical pressure trace for a 50 nm Al/Teflon confined burn.

(pps), and sample rates for tests with nanoscale Al were 100,000 pps.

A typical pressure trace is displayed in Fig. 6. Peak pressure, pressure rise time, pressurization rate, and pressure wave propagation rate were determined from the pressure history data for the fourth sensor. This sensor location was chosen for detailed analysis because at this location the reaction achieved steady state and yielded the most consistent data. Fig. 6 shows that peak pressure was found as the maximum pressure recorded. This value is directly related to the amount of gas produced during reaction which has an impact upon the flame propagation.

The rise time is the time difference between the maximum pressure and the initial rise in pressure. The rise time is a good indication of the order of magnitude for the reaction time and is sometimes referred to as the characteristic reaction time.

The pressurization rate is the slope of the increasing pressure versus time curve and is taken over the most constantly increasing segment of that curve (i.e., from 5 to 95% peak pressure) as seen in Fig. 6. The pressurization rate can give insight to the amount of gas released over a specific time. For example, a slower pressurization rate can mean a slower release of gases in the reaction. This coupled with the pressure rise time can give a good indication of the amount of gas released and the time scale of gas being released for a reaction.

The pressure wave propagation rate is found using the known distance between the pressure sensors and the difference between arrival times (point of first rise for each sensor as depicted in Fig. 6) of a sensor and its preceding sensor. The pressure wave propagation indicates how fast the pressure is moving through the confined space and can be compared to the optical wave propagation (i.e., flame speed determined from the high-speed camera tracking the leading edge of the flame front). It is noted here that there was no synchronization between the pressure and the optical propagation waves, such that only total propagation rates can be determined.

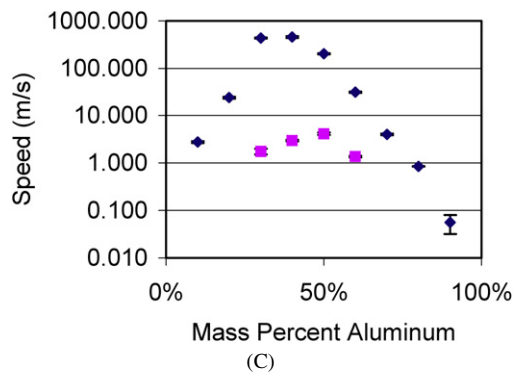
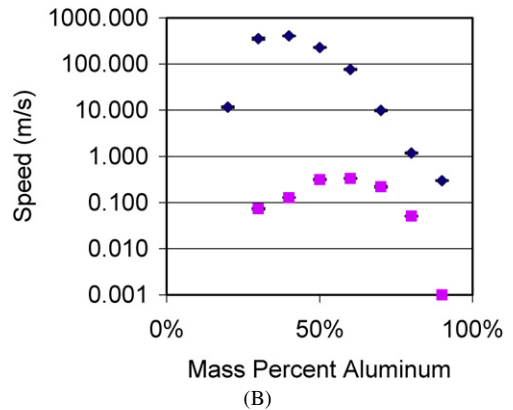
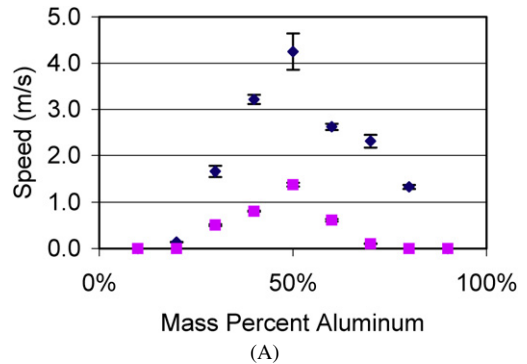


Fig. 7. Flame propagation speeds in open configurations: (A) Al/Teflon; (B) Al/MoO₃/Teflon; (C) Al/MoO₃. The diamonds represent nano-Al while the squares represent micrometer Al. Graphs presented in (B) and (C) have a logarithmic scale.

3. Results

3.1. Flame propagation in open configurations

The flame propagation speeds in open configurations are displayed in Figs. 7A–7C. Error bars are provided but may be smaller than the data point marker. These error bars represent the reproducibility of the measurements. Each data point is an average of 7–8 experiments. Peak flame speeds of 4.25, 410.64,

Table 2
Open burning flame speeds as a function of Al content and reactant composition

Percent Al	1–3 μm Al		
	Al/Teflon Velocity (m/s)	Al/MoO ₃ /Teflon Velocity (m/s)	Al/MoO ₃ Velocity (m/s)
10%	0.000	0.000	0.000
20%	0.000	0.000	0.000
30%	0.507	0.073	1.739
40%	0.808	0.127	2.953
50%	1.382	0.316	4.116
60%	0.612	0.334	1.356
70%	0.105	0.221	0.000
80%	0.000	0.051	0.000
90%	0.000	0.001	0.000

and 456.56 m/s were obtained for the nano-Al samples of Al/Teflon, Al/MoO₃/Teflon, and Al/MoO₃ composites, respectively. Peak flame speeds of 1.38, 0.33, and 4.12 m/s were found for the micrometer Al samples of Al/Teflon, Al/MoO₃/Teflon, and Al/MoO₃, respectively. The data are tabulated in Table 2.

3.2. Flame propagation in confined configurations

Figs. 8A–8C show the confined flame speed measurements. Error bars are provided but may be smaller than the data point marker. These error bars represent the reproducibility of the measurements. Each data point is an average of 7–8 experiments. Composites with the 50-nm Al particles exhibited peak flame speeds of 837, 957, and 960 m/s for the Al/Teflon, Al/MoO₃/Teflon, and Al/MoO₃, respectively. The 1–3 μm Al experiments yielded peak flame speeds of 348, 164, and 244 m/s for the respective composites of Al/Teflon, Al/MoO₃/Teflon, and Al/MoO₃, respectively. The data are tabulated in Table 3.

Each composite exhibits a significant increase in flame speed with decrease in particle size. The nano-Al experiments yielded similar peak flame speeds at an optimal ratio of 40% mass Al. Pressure data were obtained at the equivalence ratio corresponding with the highest flame speed and is displayed in Table 4 along with optical and pressure wave propagation speeds.

The faster rise times, pressurization rates, and wave speeds are associated with the composites containing 50-nm Al particles. One interesting observation is the slower optical and pressure propagation rates in the nano-Al/Teflon reaction, despite yielding the highest pressure and fastest pressurization rate.

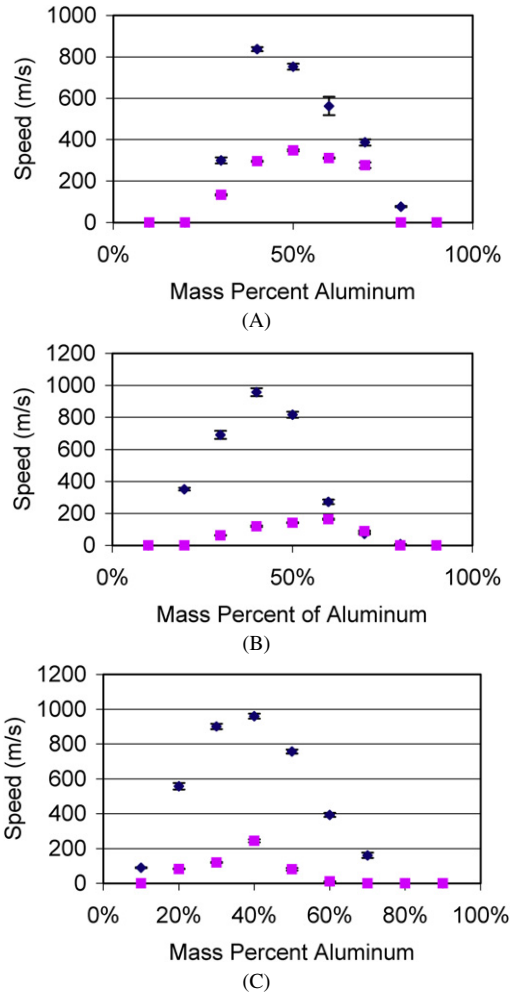


Fig. 8. Flame propagation speeds in confined configurations: (A) Al/Teflon, (B) Al/MoO₃/Teflon, (C) Al/MoO₃. The diamonds represent nano-Al while the squares represent micrometer Al.

4. Discussion

4.1. Open burning configuration

In each case the flame speed increases significantly with the decrease in particle size. The most significant impacts on flame speed with decreasing particle sizes were seen in the composites that contained MoO₃. The mixture containing MoO₃ produced a 100-fold increase in flame speed at the optimal composition compared to a factor of only 3 for the Al/Teflon reaction at its optimal composition.

The reduced flame speed associated with the open burning of Al/Teflon may be attributed to liberated gases escaping the reaction zone. These open tray experiments do not trap gaseous intermediates or prod-

Table 3
Confined burning flame speeds as a function of Al content and reactant composition

Percent Al	50 nm Al			1–3 μm Al		
	Al/Teflon	Al/MoO ₃ /Teflon	Al/MoO ₃	Al/Teflon	Al/MoO ₃ /Teflon	Al/MoO ₃
	Velocity (m/s)	Velocity (m/s)	Velocity (m/s)	Velocity (m/s)	Velocity (m/s)	Velocity (m/s)
10%	0.000	0.000	88.859	0.000	0.000	0.000
20%	0.014	351.469	557.249	0.000	0.000	82.755
30%	299.629	690.551	901.551	133.249	62.229	120.070
40%	837.498	957.216	960.234	295.848	119.623	244.019
50%	752.048	816.436	756.400	348.279	141.350	80.918
60%	562.282	272.447	393.389	310.887	163.902	11.103
70%	386.663	72.080	160.627	276.759	89.263	0.000
80%	76.915	8.525	0.000	0.000	0.000	0.000
90%	0.000	0.000	0.000	0.000	0.000	0.000

Table 4
Pressure (*P*) and propagation (prop.) results from confined experiments

Al size	Mass% pure Al	Composition	Mass (mg)	Peak <i>P</i> (MPa)	Rise time, <i>t_p</i> (μs)	<i>P</i> rate (MPa/s)	Estimated heating rate, 2000 K/ <i>t_p</i> (10 ⁶ K/s)	<i>P</i> prop. rate (m/s)	Optical prop. rate (m/s)
50 nm	40	Al/Teflon	201.2	10.75	84	181746	23.8	762	838
	40	Al/MoO ₃ /Teflon	211.8	5.45	78	95877	25.6	847	958
	40	Al/MoO ₃	196.6	1.46	63	44922	31.7	823	960
1–3 μm	50	Al/Teflon	400.6	4.18	784	29969	2.6	186	348
	60	Al/MoO ₃ /Teflon	384.2	0.38	2105	242	0.95	59	164
	40	Al/MoO ₃	362.7	0.82	245	3336	8.2	240	244

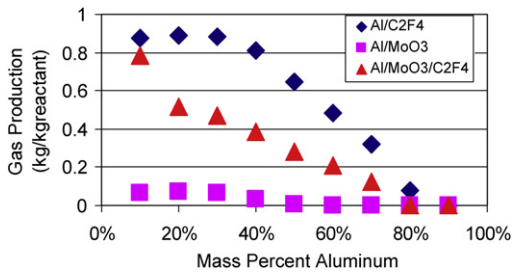


Fig. 9. Gas generation in the Al/Teflon, Al/MoO₃/Teflon, and Al/MoO₃ reactions. Values determined using the REAL Code (Tim Tec, LLC) chemical equilibrium program.

ucts, thus a large portion of energy in the reaction escapes with the liberated gases instead of contributing toward accelerating the flame front. Thermodynamic equilibrium calculations using REAL (Tim Tec, LLC) code assuming thermal equilibrium exists during the reaction indicate the quantity of gas production as a function of aluminum content for the binary and ternary mixtures (Fig. 9).

For unconfined burning environments, adding Teflon to the mixture produces fluorine gas that escapes to the surroundings and does not contribute to the reaction and the convective mode of energy propagation. Teflon decomposes at 803 K, which is prior

to the Al ignition temperature (i.e., >850 K). With gaseous intermediates escaping, it is likely that incomplete combustion occurs as only a portion of the oxidizing agent is reacting. Therefore, the addition of Teflon to unconfined reactions enables gas to escape prior to reaction and results in incomplete combustion and slower flame speeds. These results imply that achieving high flame speeds in an open environment can be accomplished using nano-aluminum particles combined with a metallic oxide that does not produce a significant amount of gas.

4.2. Effects of confinement

In confined configurations, the gases generated cannot significantly escape and enhance the convective mode of energy propagation. Under confinement the composites containing Teflon produce higher peak pressures as expected with the increased gas generation. Also, more fluorine gas may be available for reaction with Al because the gas is unable to escape. Therefore, more complete combustion may also contribute to increased energy content and faster flame speeds.

Confining the reaction enables fluorine and oxide gases to remain within the reactant matrix, thereby

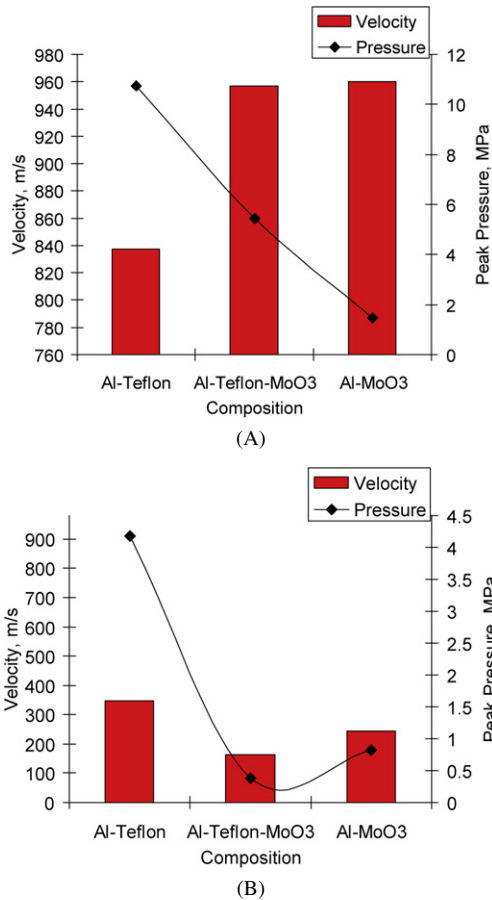


Fig. 10. Flame velocity (represented as a bar graph) and peak pressure (represented as data points with a trend line curve) for different reactive mixtures. (A) Nano-Al and (B) micrometer-Al.

leading to more complete reaction and promoting increases in flame speed. However, the nano-Al–MoO₃ reaction still produces the fastest flame speed even with significantly less gas generation and pressure increase (Fig. 10A). The Al–MoO₃ mixture contains an overall lower heat of combustion (Fig. 1), but a higher adiabatic flame temperature (Al–MoO₃ 3793 K; Al–Teflon 3431 K; computed using REAL code including alumina content as a reactant). In this way, the high flame speed may be promoted by the higher reaction temperatures. The increased gas generation associated with Al–Teflon and Al–Teflon–MoO₃ did not translate to increased flame speeds when compared with Al–MoO₃ (and negligible gas generation). The nano-Al/Teflon reaction exhibited the slowest flame speed as well as the highest peak pressure when confined (Fig. 10A). For micrometer Al there is some correlation between generated pressure and flame speed (Fig. 10B).

These results imply that the direct relationship between generated gas pressures and flame speeds does not generally exist when comparing different oxidizers (Fig. 10). For nano-Al (Fig. 10A) a pressure threshold may occur at roughly 10 MPa such that further increases in pressure within the confined arrangement do not lead to increased flame speed. For micrometer-Al particles (Fig. 10B) the drop in peak pressure and velocity when Teflon is included with MoO₃ may be indicative of an incomplete reaction, as shown in [20].

5. Reaction mechanism

There are currently three mechanisms that are used to describe and interpret the reaction of nano-Al particles:

1. Diffusive oxidation mechanism in which Al and oxygen diffuse toward each other through growing oxide shell surrounding Al particles. This mechanism was justified in [22] experimentally and in [23] using modeling. The heating rate in these experiments was estimated as 10^3 K/s. This mechanism requires at least 1 s for complete oxidation to occur, while the estimated reaction time in our experiments (Table 4) is four orders of magnitude smaller for nanoparticles and three order of magnitude smaller for micrometer Al particles. Thus, this mechanism cannot be operative in our experiments.
2. Recently [14,15,24], we predicted theoretically and confirmed experimentally that fast oxidation (i.e., heating rates 10^6 – 10^8 K/s) of Al nanoparticles react according to the melt-dispersion mechanism (Fig. 11). It was shown that at fast heating rates the alumina shell for nanoparticles does not break until Al melts. The main geometric parameter that determines stresses in the Al core–shell system is the ratio of Al core radius R to oxide thickness δ , $M = R/\delta$. It was found [14,15,24] that for $M < 19$, the entire Al particle melts before oxide shell fracture. Fast melting of Al is accompanied by a 6% volume expansion which creates high dynamic pressures (1 to 3 GPa) in the liquid core. Pressure of such magnitude overloads the alumina shell with the hoop stresses σ_h that exceed the ultimate strength of alumina σ_u and causes the shell's dynamic fracture and spallation. After oxide spallation, pressure within the liquid Al remains unchanged while at the bare Al surface the pressure is of the order of 10 MPa only due to surrounding gas pressure and surface tension. Then an unloading wave propagates from the surface to the center of the parti-

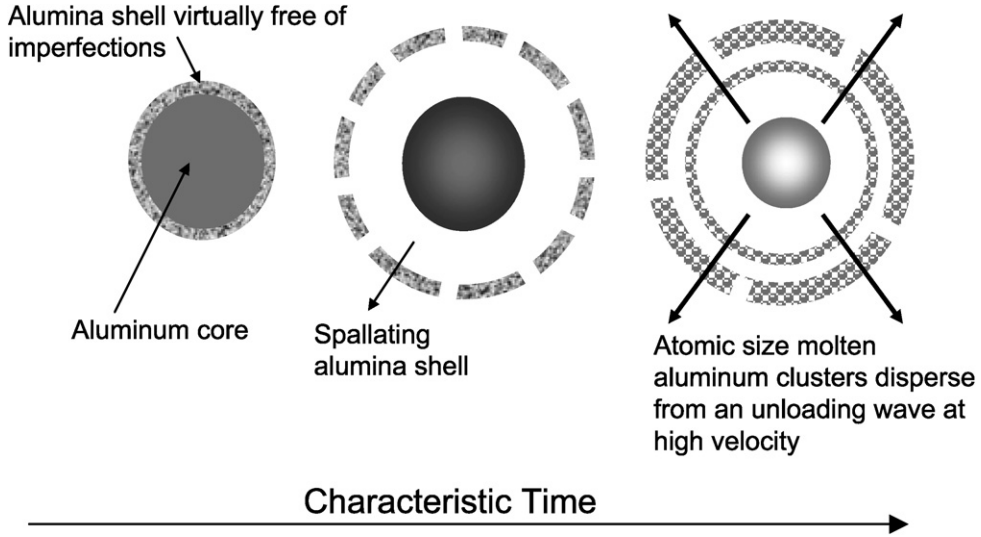


Fig. 11. Schematic diagram illustrating that nanoparticles react via a melt-dispersion mechanism. Initially melting of Al creates huge internal pressures followed by spallation of the oxide shell exposing the molten core and generating an unloading pressure wave which disperses small Al clusters.

cle and creates a tensile pressure at the particle center of 3 to 8 GPa. Such a pressure exceeds the strength (cavitation limit) of molten Al, and disperses the liquid Al into small bare clusters that fly at a high velocity (100–250 m/s). Oxidation of these clusters is not limited by diffusion through initial oxide shell. Currently [24], measured flame rates are in good correspondence with the melt-dispersion mechanism predictions for particles with diameter $D \leq 120$ nm and $M \leq 35$ (Fig. 12). Predictions based on elasticity theory suggest that the melt-dispersion mechanism may also be operative for micrometer size particles [15]. Also, the question of whether or not this mechanism operates for reactions other than oxidation has not been considered before.

Although the measurements of the optical flame speed and peak pressure propagation speed were not synchronized, the optical front is assumed to be ahead of the peak pressure front. The reasons for this assumption are that the optical front is faster than the peak pressure front and that in Sanders et al. [25], this was the case for reaction of Al with four different oxidizers including MoO_3 . Pressure starts to grow at or slightly ahead of the optical flame front and the pressure rise time can be a rough estimate for the Al reaction time in fast reaction regions between optical and pressure peak fronts. Dividing estimated flame temperature increases on the order of 2000 K by pressure rise time, estimates were obtained for the heating rate shown in Table 4. Our estimates in [15,26] show that the heat-

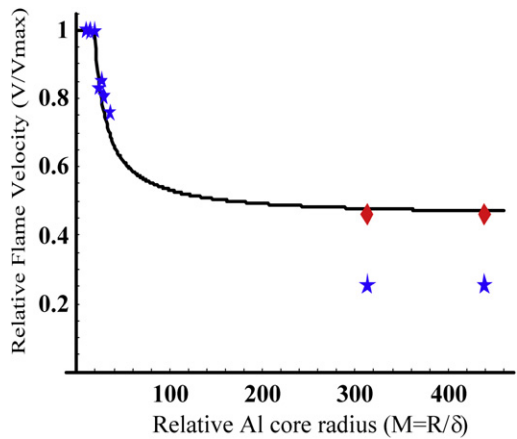


Fig. 12. Relative flame velocity V/V_{max} vs relative Al core radius $M = R/\delta$ for Al/ MoO_3 mixtures (stars) and Al/Teflon mixtures (diamonds). The line represents the volume fraction of melt, f , necessary to fracture of the oxide shell from Eq. (6). Data for $M < 35$ are from [24].

ing rate required to activate the melt-dispersion mechanism is equal or higher than 10^6 K/s. It follows from Table 4 that all mixtures satisfy this condition. Thus, choosing between diffusion and melt-dispersion mechanisms, all reactions in Table 4 in confined configurations likely occur through the melt-dispersion mechanism. For other experiments for which pressure rise time is not available, an alternative estimate is used [26] based on the flame speed. Thus, if the flame rate exceeds 10 m/s, self-heating provides high enough heating rates for activation of the

melt-dispersion mechanism. Based on this approximate criterion, data for all experiments in confined configurations (for all reactions and for both nano- and micrometer-scale Al), if ignited, occur via the melt-dispersion mechanism. For open configurations, the melt-dispersion mechanism is expected for Al nanoparticle mixtures with MoO₃ (20–60% of Al) and with MoO₃ and Teflon (20–70% of Al). All other mixtures with Al nanoparticles as well as all formulations with micrometer Al particles react according to the diffusion mechanism.

3. In [27,28], a diffusion-based oxidation model is developed which takes into account phase transformations in the alumina shell. Transformation of amorphous alumina to γ -alumina is accompanied by 17% volume decrease. The key points of this model which permit short oxidation times are the following. First, phase transformation for nanoparticles occurs at 0.1 μ s time scale at environmental temperatures of 1300–1350 K. Second, it is assumed that reduction in volume by 17% results in 17% bare Al area. Third, this area is kept bare until the oxide shell grows up to 5 nm, while exposed Al must be covered immediately by new growing oxide shell. This model is calibrated and checked against experiments for very slow heating (up to 5 K/min for nanoparticles and 40 K/min for micrometer particles [27,28]) but then extrapolated to very fast heating rate of 10^{10} K/s (for nanoparticles, temperature increased by 1000 K during 0.1 μ s). Even for fully physically based models such a far away extrapolation is doubtful; however, the model in [27] is purely phenomenological, without consideration of nucleation, with simplified treatment of growth and neglected effect of stresses. Also:
 - (a) Based on kinetic data in [29] complete phase transformation time at temperatures 1573 K is 7.9×10^{-2} s which is six orders of magnitude larger than obtained in [27]. This means that phase transformation cannot occur during the reaction duration.
 - (b) Even if phase transformation occurs, it occurs in [27] after melting and several hundred degrees above the melting temperature. Thus, fracture of oxide shell caused by melting must occur and the melt-dispersion mechanism can operate.
 - (c) While fracture during fast transformation is the key process in [27], no stress, mechanics of phase transformations, and fracture models were presented. An assumption that reduction in volume by 17% results in 17% bare Al area (i.e., occurs at constant oxide thickness) contradicts thermodynamics of

phase transformation under nonhydrostatic conditions. For amorphous to crystal phase transformation, the volume change is prescribed, while change in shape should maximize the thermodynamic driving force for phase transformation [30,31]. Since the oxide shell is under large tensile hoop stresses, contraction by 17% in hoop directions produces large negative transformation work that reduces significantly the driving force for phase transformation. In an alternative scenario, when the thickness of the shell reduces during transformation by more than 17%, the shell expands in hoop directions and transformation work is positive. This increases the thermodynamic driving force for phase transformation and accelerates transformation kinetics. Thus, according to the principle of the maximum driving force for phase transformation or minimum of transformation time [30,31], the second scenario should occur, in contrast to the assumption in [27]. Since tensile stresses relax due to shape change during the phase transformation, fracture of the shell may not occur at all. The energy of the particle with a continuous shell and stresses relaxed due to phase transformation is lower than the energy of the particle with a fractured shell by energy of fractured surfaces.

- (d) We found in [24] that for various Al particles with $M < 19$, the flame speed reaches a maximum value of 950 m/s, which corresponds to a reaction time of 10 μ s [15]. Currently, our X-ray analyses of those particles showed that for Al particles of 120 nm in diameter and an oxide shell of 4 nm (i.e., $M = 14$), initially the shell was in γ phase. For smaller particle size and oxide shell, the shell was initially amorphous. Also, ignition times for nano-Al particles with an oxide shell smaller than 3.4 nm (which are in the amorphous state) and from 4.5 to 7.7 nm (which are in the γ phase) are approximately the same, provided that $M < 19$ [4,15]. Thus, independent of whether the shell is in amorphous or gamma phase (i.e., whether phase transformation from amorphous to gamma phase occurs or not), nanoparticles exhibit the same maximum possible reactivity in terms of ignition delay time, flame rate, and, consequently, reaction time. These results show that phase transformation is not the reason for short reaction times, which is in contradiction with the phase-transformation-based model in [27]. The only reason why

model [27] can give short ignition time is the presence of the phase transformation from amorphous to gamma phase, which fractures the oxide shell. Without phase transformation, the model in [27] is the diffusion-based model similar to the model in [23] and should give reaction time of the order of 1 s, instead of 10–100 μ s observed experimentally.

- (e) Predicted ignition time for nanoparticles in [27] is three orders of magnitude smaller than in reaction time experiments in [32,33]. It is written in [32] that the ignition time is approximately 0.6 of the reaction time, in accordance with previous experiments. Since we are talking about three orders of magnitude discrepancy, even large error in the above factor does not change our conclusion. This is, however, not a major problem. The model in [27] has enough fitting parameters in exponential functions and slight changes in these parameters may adjust the calculation of oxidation time.

Summarizing, although no existing mechanism is strictly proved, the melt-dispersion mechanism is the only mechanism which does not demonstrate major contradictions and possesses various experimental confirmations.

5.1. Relative flame speed versus relative particle size M : Theoretical predictions

Here we compare predictions for the flame speed based on the melt-dispersion mechanism with obtained experimental data. Some preliminary results are presented in [34]. In [24], Eqs. (6) and (7) for the flame propagation speed V were derived for the case when fracture of the shell occurs at a temperature equal to the melting temperature of Al $T_m = 933.67$ K:

$$V/V_{\max} = f, \quad (6)$$

$$f = (-B + \sqrt{B^2 - 4AC})/2A, \quad \text{for } 0 < f \leq 1, \quad (7)$$

where f is the volume fraction of melt in Al core necessary to fracture of the oxide shell, V_{\max} is the maximum velocity that can be achieved for relatively small M (see Fig. 12) in the same experimental setup, for the same mass density of the powder, and for the same oxidizer, and parameters A , B , and C are defined in equations:

$$A = 6\delta\varepsilon^m \Delta K (2 + m^3) M G_2 K_2, \quad (8)$$

$$m = 1 + 1/M,$$

$$B = \Delta K m^2 (\delta(1 + M)p_g + 2\Gamma_2)(2G_2 - 3K_2) + 6\delta(2 + m^3)M(\varepsilon^m K_S + \Delta\alpha \Delta K \Delta T)G_2 K_2 - \delta\Delta K M(4G_2 + 3m^3 K_2)\sigma_u, \quad (9)$$

$$C = 6\delta(2 + m^3)M\Delta\alpha K_S \Delta T G_2 K_2 - 4(2 + m^3)\Gamma_1 G_2 K_2 + m^2(\delta(1 + M)p_g + 2\Gamma_2) \times (2K_S G_2 - 3(K_S + 2G_2)K_2) - M\delta\sigma_u(3K_S K_2 m^3 + 4G_2(K_S + (m^3 - 1)K_2)). \quad (10)$$

In Eqs. (8)–(10), $G_2 = 149.5$ GPa and $K_2 = 234.8$ GPa are the shear and bulk moduli of the oxide shell, $K_S = 71.1$ GPa is the bulk modulus of solid Al, $\Delta K = -29.8$ GPa is the difference in bulk moduli between liquid and solid Al, $3\varepsilon^m = 0.06$ is the volumetric expansion during Al melting, ΔT is the difference between the melting temperature T_m and the passivation temperature, T_0 , at which the initial oxide shell was formed, Γ_1 and Γ_2 are the surface tensions at the aluminum–alumina interface and alumina–gas interface that appears during the reaction ($\Gamma_1 = \Gamma_2 = 1.05$ GPa nm), $\Delta\alpha = 2.254 \times 10^{-5}$ K $^{-1}$ is the difference in linear thermal expansion coefficients between solid Al and alumina and p_g is the pressure of the gas. All the above parameters are evaluated at melt temperature and collected in [15].

If only M is varied in flame propagation experiments, flame velocity for relatively small M reaches its maximum value V_{\max} , which is independent of M (Fig. 12). We use this result to determine V_{\max} experimentally. In some range of parameters, the relative flame rate V/V_{\max} is independent of the setup, oxidizer, mass density, because this information is included in V_{\max} . Indeed, experimental points in Fig. 1 were obtained using several setups with different tube lengths, diameters, and location of the pressure sensors. From a physical perspective, Eq. (6) can be interpreted as the entire molten Al which induces fracture of the oxide shell and participates in the MDM and reaction during time scales of ~ 10 – 100 μ s while the flame front passes through chosen particles. The residual nondispersed Al core reacts over longer time scales and does not contribute to V . While it is expected (based on melt-dispersion mechanism) that relative flame rate V/V_{\max} is an increasing function of the concentration of melt f necessary to fracture the oxide shell, coincidence between V/V_{\max} and f is not currently justified theoretically and was obtained empirically (Fig. 12) for nanoparticles with $M < 35$ for Al/MoO $_3$ mixture. On the other hand, Eq. (7) for f was obtained theoretically from the fracture criterion for oxide shell, $\sigma_h = \sigma_u$. In Fig. 12, the solid line represents prediction based on Eqs. (6) and

Table 5
Flame velocities in m/s for Al/Teflon and Al/MoO₃ mixtures

Percent Al	Al/Teflon			Al/MoO ₃		
	V _{max}	V _{mic}	V _{mic} /V _{max}	V _{max}	V _{mic}	V _{mic} /V _{max}
20%				557.2	82.8	0.149
30%	299.6	133.2	0.444	901.6	120.1	0.133
40%	837.5	295.8	0.353	960.2	244.0	0.254
50%	752.0	348.3	0.463	756.4	80.9	0.107
60%	562.3	310.9	0.407			

(7) for f vs M for $T_0 = 300$ K, $\sigma_u = 11.33$ GPa, and $\delta = 4$ nm. It is taken into account that f very weakly depends on δ and the value for ultimate strength of alumina σ_u was obtained in [15] by fitting to experiment the point $M = 19$ at which $f = 1$ and V/V_{\max} is independent of M . It was concluded in [15] that σ_u is equal to the evaluated value of theoretical strength $\sigma_{th} = E/30 = 11.33$ GPa, where E is the Young modulus.

Equations (6) and (7) connect two scales: nano-scale size of Al particles and flame speed at the macroscopic scale. Information on flame propagation mode and specific set up is decoded in V_{\max} , while geometric, thermomechanical, and surface properties of Al nanoparticles and condition of their synthesis (T_0) contribute to melt concentration f .

Equations (6) and (7) predict that even for large micrometer-scale particles the amount of molten Al can provide a high flame speed if entire melt participates in melt-dispersion mechanism and reaction. However, Eqs. (6) and (7) do not take into account other processes (e.g., cavitation, dispersion, and collision of nanoclusters with an oxidizer or fluorine) which can limit the value M for which Eqs. (6) and (7) are in agreement with experimental data.

5.2. Relative flame rate versus relative particle size M : Comparison with experiments

Table 5 contains flame velocity results from experiments for Al/Teflon and Al/MoO₃ mixtures from Table 3 necessary for comparison with theoretical predictions from Eq. (6), i.e., for which the melt-dispersion mechanism is expected. Since for nano-Al particles $M = 14.2 < 19$, then V_{\max} is the flame rate for nano-Al particle mixtures, while V corresponds to flame rate V_{mic} for micrometer Al particle mixtures.

Experimental data points corresponding with V/V_{\max} versus M for Al/Teflon and Al/MoO₃ mixtures are presented in Fig. 12 with data symbols. In addition to parameters for actual particles given in Table 1, also considered for comparison are small deviations from the Al content given by the manufacturer, e.g., $C = 0.986$ (also specified in Table 1). Such a small deviation leads to a decrease in M and an increase in

Table 6

Estimated values of pressure in Al core and maximum particle velocity at the instant of fracture of oxide shell for Al particles under study

Particle diameter, D	M	δ (nm)	p_0 (MPa)	v (m/s)
1 μm	312	1.6	85.3	4.8
1 μm	438	1.1	64.7	3.5
3 μm	312	4.8	79.6	4.6
3 μm	438	3.4	58.8	3.3
50 nm	14.2	1.6	1580	92.5

δ by 40%. However, changes in M from 438 to 312 do not significantly change the theoretical values for the volume fraction of melt necessary to fracture the oxide shell (Fig. 12). Thus, inaccuracy in C values for micrometer particles provided by the manufacturer does not affect a comparison between theory and experiment.

Note that Eq. (6) is applicable for an optimal equivalence ratio only, i.e., for Al content corresponding to maximum value of V/V_{\max} . Thus, $V_{\text{mic}}/V_{\max} = 0.254$ for Al/MoO₃ mixtures and $V_{\text{mic}}/V_{\max} = 0.463$ for Al/Teflon mixtures (both for 40% Al content) must be compared with the predictions from Eq. (6). It is clear from Fig. 12 that the value V_{mic}/V_{\max} for Al/Teflon is in good correspondence with the relationship $f(M)$ for the same $\sigma_u = 11.33$ GPa in the range $M = 312$ –438. This result *strongly supports* the melt-dispersion mechanism for 1- to 3- μm particles and expands by more than an order of magnitude the range of M for which Eq. (6) is applicable.

According to Fig. 12, the entire liquid Al participates in reaction for an optimal Al/Teflon mixture. This means that the *cavitation of molten Al (and collision and reaction rates of Al clusters with gaseous fluorine) is not a limiting process*. Based on this conclusion, we can evaluate at least the upper bound for the cavitation threshold. To calculate the pressure in the Al core at the instant when the oxide shell fractures, we used Eq. (6) in our paper [15]. The measured peak pressure $p_g = 4.2$ MPa is taken into account, which contributes additively. Results from these calculations are presented in Table 6.

In order to estimate the cavitation threshold p_c , we will use Eq. (22) from [15] for the pressure in the Al core necessary to cause cavitation in an Al sphere; repeated here as equation

$$p_0 = \frac{p_c \bar{t}_s + p_g}{1 - \bar{t}_s}, \quad (11)$$

where \bar{t}_s is the ratio of the time of oxide shell fracture to the acoustic time during which an unloading wave reaches the particle's center. It is shown in [15] that when the unloading wave reached the center of a particle, the relative radius $\bar{r} = r/R$ at which tensile pressure reaches its maximum (and remains constant for smaller radii) is equal to \bar{t}_s . Thus, Eq. (11) can be substituted with

$$p_c = \frac{p_0(1 - \bar{r}) - p_g}{\bar{r}}. \quad (12)$$

The interface between the solid Al sphere and the surrounding liquid Al layer is the best nucleation site for heterogeneous bulb nucleation or cavitation due to decohesion of melt from solid. That is why we assume that the relative radius of solid–liquid interface is equal to \bar{r} . Then \bar{r} is related to the volume fraction of the melt f by equation:

$$f = 1 - \bar{r}^3, \quad \text{i.e.,} \quad \bar{r} = \sqrt[3]{1 - f}. \quad (13)$$

For maximal f achieved for micrometer Al particles, $f = 0.463$, such that $\bar{r} = 0.81$. Taking from Table 6 the maximum $p_0 = 85.3$ MPa (or the minimum $p_0 = 58.8$ MPa) and $p_g = 4.2$ MPa, one can evaluate the cavitation threshold as $p_c \leq 15$ MPa (or $p_c \leq 9$ MPa). These estimates are significantly lower than 1 GPa, which was evaluated in paper [15] for homogeneous bulb nucleation. Knowledge of the nucleation threshold is extremely important since it allows us more precise estimation of the possibility of extension of the melt-dispersion mechanism for larger particles based on methods suggested in [15]. For large M , Eq. (6) can be significantly simplified [15] as shown in equation:

$$f = \frac{J\sigma_u - \Delta\alpha(T - T_0)}{\varepsilon^m + (\alpha_1^m - \alpha_1^s)(T - T_m)}, \quad (14)$$

where $J = (4G_2 + 3K_2)/18G_2K_2 = 0.0021$ and α_1^m and α_1^s are the thermal expansion coefficients of Al in molten and solid state. Equation (14) is derived for arbitrary T at the fracture instant. For $T = T_m$ (like in Eq. (6)), Eq. (14) simplifies to $f = (J\sigma_u - \Delta\alpha\Delta T_0)/\varepsilon^m$. The concentration f is independent of M , as in Fig. 12 for large M .

For an optimal Al/MoO₃ mixture, the experimental ratio $V_{\text{mic}}/V_{\text{max}}$ for Al/MoO₃ is 55% of the prediction based on Eq. (6) plotted in Fig. 12. Let us discuss the possible reasons for this discrepancy. For

all experiments tabulated in Table 5, the flame and heating rates are high enough to activate the melt-dispersion mechanism. That is why it is reasonable to assume that for all the above experiments the same amount of melt in Al core causes oxide shell fracture and disperses. Then the efficiency of reaction between dispersed bare Al clusters and fluorine or oxygen is responsible for the reduced flame speed in comparison with the flame speed for an optimal Al/Teflon mixture. The collisions of liquid clusters with solid or gaseous oxidizer or gaseous fluorine may be a factor limiting reaction and flame rate, because (as will be discussed below), the velocity of the flying Al clusters for micrometer particles is much slower than for nanoparticles. Decomposition of Teflon produces a lot of fluorine gas under high pressure (4.2 MPa versus 0.8 MPa for Al/MoO₃ mixture) that has higher collision and reaction rates with slow Al nanoclusters and provides higher flame speeds than for Al/MoO₃ mixture. This means that it is necessary to improve collision conditions between Al nanoclusters and oxygen for an optimal equivalence ratio for Al + MoO₃ mixtures. It may be done by reducing the distance between Al and oxidizer particles and optimization of shape of oxidizer particles, by promoting sublimation of MoO₃, as well as by increasing clusters' velocity. For nonoptimal equivalence ratio, the reduction in flame speed is related to incomplete reaction between dispersed bare Al clusters and fluorine or oxygen.

To address the question of probability of collision between Al nanoclusters and oxidizer or fluorine, we evaluate particle velocity v at the instant when the rarefaction wave reached the particle's center. Numerical analysis for the evolution of the velocity field in molten particle is presented in [15]. The maximum value of particle velocity will be evaluated using an analytical expression in Eq. (14) from [15]. In this equation, the relative shell fracture time \bar{t}_s is substituted with \bar{r} , similar to transformation from Eq. (11) to Eq. (12), i.e.,

$$v_m = \frac{p_0 - p_g - 2\Gamma/R}{2\rho c\bar{r}}. \quad (15)$$

Here $c = 4166$ m/s is the sound velocity in Al melt, $\rho = 2380$ kg/m³ is the mass density of the melt, $\Gamma = 1.05$ GPa nm is the Al–gas interface energy, and \bar{r} corresponds to the point where pressure and velocity reach their maximum, i.e., $\bar{r} = 0.81$ in our case. Calculated particle velocities are shown in Table 6. For micrometer particles, the particle velocities are approximately 20 to 30 times slower than for nanoparticles, and their collisions with solid or gaseous oxidizer or gaseous fluorine may be a factor limiting reaction and flame speed.

To summarize, comparison of experimental data with theoretical predictions strongly supports the va-

lidity of the melt-dispersion mechanism for 1- to 3- μm Al particles for fluorination and oxidation. The range of relative particle sizes M , for which the equation $V/V_{\text{max}} = f$ is valid, is extended from the $M < 35$ in [24] to $M < 312\text{--}438$ in this paper for fluorination. For micrometer particles, the main physical parameters for the melt-dispersion mechanism (nanocluster velocity, pressure in molten particle, and cavitation threshold) have been estimated.

6. Directions for improvement of the effectiveness of Al burning

For Al/MoO₃ mixtures, the probability of collisions of nanoclusters with gaseous or solid oxidizers is one of the factors limiting reaction time and flame speed. Reaction time may be decreased:

- by reducing distance of Al and oxidizer particles,
- by optimization of the shape of oxidizer particles,
- by promoting sublimation of MoO₃,
- and by increasing velocity of nanoclusters.

However, Eq. (6) predicts that this will increase V/V_{max} up to 0.463 only. In addition, one can apply some methods suggested in [15]; which are now much more justified by the results obtained in the current work. Indeed, for Al/Teflon mixtures we found that cavitation, slow cluster velocity, and shell strength are not limiting parameters. However, for Al/MoO₃ mixtures, velocity of nanoclusters is a limiting parameter. Two parameters suggested in [15], namely oxide shell thickness δ and temperature T_0 at which initial oxide shell is formed, can be increased to promote the melt-dispersion mechanism. Thus, oxide thickness can be increased at least to 7.7 nm without decreasing its possible maximum strength (see [15]). This will not significantly increase V/V_{max} : to 0.577 for 1- μm particles and to 0.493 for 3- μm particles. However, pressure and particle velocity grow to 123.8 MPa and 7.5 m/s for 3- μm particles and to 367.2 MPa and 24.1 m/s for 1- μm particles. This may essentially increase the collision and reaction rate, which is important for Al/MoO₃ but not for Al/Teflon. Note that an oxide shell thicker than 4–5 nm is highly probable in crystalline γ phase rather than in an amorphous state of alumina. However, the thicker shell does not affect ignition time for $M < 19$ [4,15].

Temperature at which initial oxidation occurs is a more influential parameter. Increase in T_0 creates compressive stresses in oxide shell and tensile stresses in Al core, thus delaying the shell fracture and promoting the melt-dispersion mechanism. If for $\delta = 7.7$ nm we increase T_0 from 300 K to 635 K for 1- μm particles, we obtain significant improve-

ment: $V/V_{\text{max}} = 0.988$ and $v = 78.5$ m/s. Note that pressure is practically unaffected by T_0 , because for micrometer particles it is approximately determined by equation [15]:

$$p_0 = 2\sigma_u \frac{\delta}{R} + \frac{2(T_1 + T_2)}{R} + p_g. \quad (16)$$

If we increase T_0 to 730 K for 3- μm particles, we obtain $V/V_{\text{max}} = 0.990$, $v = 27.6$ m/s. We intentionally keep a small residual solid Al in order to promote heterogeneous nucleation solid–melt interface and reduce significantly the cavitation threshold. If the increase in T_0 and corresponding effect can be realized in experiments, the micrometer-scale particles will exhibit the same performance as nanoscale particles. Limitations on maximum possible T_0 are related to decohesion of the oxide shell at room temperature [15] and possible sintering of particles at high temperature. Also, cooling from T_0 to room temperature should be fast to avoid relaxation of internal stresses. Note that currently nanoscale particles are 30 to 50 times more expensive than the micrometer particles. Current work demonstrates that the melt-dispersion mechanism revealed for the nanoscale can be extended to micrometer-scale particles. An important point is that the reaction is still governed at the scale of molten nanoclusters. However, these nanoparticles are produced in situ for free during the dispersion of micrometer-scale particles rather than produced by expensive technology.

7. Conclusions

The use of fluorine as an oxidizing agent in thermite reactions yields higher heats of combustion as well as increased gas generation over metallic oxidizers. In open burn configurations the increased gas content reduces flame propagation speeds because gas liberated during the reaction escapes. In the confined state these gases are contained, promoting enhanced convection as well as more complete combustion.

These results imply that in open configurations faster flame speeds will be achieved by using oxidizers that result in low gas output reactions. In the confined configuration the faster flames speeds are achieved by using reactants that produce enough gas to enhance convection and promote complete combustion. Results from this work showed that although nano-Al and Teflon produce the highest peak pressure (and pressurization rate) in a confined reaction, the resulting flame speed is roughly 100 m/s less than the nano-Al and MoO₃ or nano-Al + MoO₃ + Teflon reaction (Fig. 10). These results imply that the direct relationship between generated gas pressures and flame speeds does not generally exist when comparing different oxidizers.

The large difference in factor of increase when confining the Al/Teflon reaction when compared to the other reactions may be achieved by a shift in mechanism from diffusion to melt dispersion. The impact of melt dispersion is observed by the difference in this factor of increase as well as the differences in flame speed when comparing the nanoscale open burns.

The obtained results generalize the melt-dispersion mechanism of oxidation of Al nanoparticles for fluorination reaction and for 1- to 3- μm diameter Al particles. The theoretically predicted relationship for the relative flame speed versus relative particle size based on the melt-dispersion mechanism agrees with experimental data for 1- to 3- μm Al particles and fluorination. The particle synthesis parameters are suggested that could be controlled to enable micrometer-scale Al particles to achieve the performance of nanoscale Al particles. Note that currently nanoscale particles are 30 to 50 times more expensive than the micrometer particles. Current work demonstrates that the melt-dispersion mechanism revealed for the nanoscale can be extended to micrometer-scale particles. An important point is that reaction is still governed at the scale of molten Al nanoclusters dispersed. However, these nanoparticles are produced in situ for free during the dispersion of micrometer-scale particles rather than produced by expensive technology.

Acknowledgments

The authors gratefully acknowledge support from the Army Research Office contract W911NF-04-1-0217 (program director Dr. Ralph Anthenien), Office of Naval Research contract N000140810104 (program director Dr. Clifford Bedford), and National Science Foundation Grant CBET-0755236 (program director Dr. Phillip Westmoreland). We are thankful for helpful discussions with Mr. Dustin Osborne regarding the experimental configuration.

References

- [1] C.E. Aumann, G.L. Skofronick, J.A. Martin, *J. Vac. Sci. Technol. B* 13 (1995) 1178–1183.
- [2] A.W. Miziolek, *AMPTIAC Newslett.* 5 (1) (2002) 43–48.
- [3] L.L. Wang, Z.A. Munir, Y.M. Maximov, *J. Mater. Sci.* 28 (14) (1993) 3693–3708.
- [4] J.J. Granier, M.L. Pantoya, *Combust. Flame* 138 (4) (2004) 373–383.
- [5] K.B. Plantier, M.L. Pantoya, A.E. Gash, *Combust. Flame* 140 (4) (2005) 299–309.
- [6] B.S. Bockmon, M.L. Pantoya, S.F. Son, B.W. Asay, J.T. Mang, *J. Appl. Phys.* 98 (6) (2005) 064903.
- [7] Y. Yang, S. Wang, Z. Sun, D.D. Dlott, *Appl. Phys. Lett.* 85 (9) (2004) 1493–1495.
- [8] N. Kubota, C. Serizawa, *J. Propul. Power* 3 (4) (1987) 303–307.
- [9] H.R. Lips, *J. Spacecraft Rockets* 14 (9) (1977) 539–545.
- [10] J. Eckert, J.C. Holzer, C.C. Ahn, Z. Fu, W.L. Johnson, *Nano Mater.* 2 (4) (1993) 407–413.
- [11] A. Revesz, *J. Mater. Sci.* 40 (7) (2005) 1643–1646.
- [12] Z. Zhang, X.X. Lu, Q. Jiang, *Physica B* 270 (3–4) (1999) 249–254.
- [13] S. Valliappan, J. Swaiakiewicz, J.A. Puszynski, *Powder Technol.* 156 (2–3) (2005) 164–169.
- [14] V.I. Levitas, B.W. Asay, S.F. Son, M.L. Pantoya, *Appl. Phys. Lett.* 89 (7) (2006) 071909.
- [15] V.I. Levitas, B.W. Asay, S.F. Son, M.L. Pantoya, *J. Appl. Phys.* 101 (8) (2007) 083524.
- [16] E.C. Koch, *Propellants, Explosives, Pyrotechnics* 27 (5) (2002) 262–266.
- [17] E.C. Koch, *Propellants, Explosives, Pyrotechnics* 27 (6) (2002) 340–351.
- [18] L.J. Parker, H.D. Ladouceur, T.P. Russell, *AIP Conf. Proc.* 505 (1) (2005) 941–944.
- [19] T. Tachibana, I. Kimura, *J. Propul. Power* 4 (1) (1988) 41–46.
- [20] D.T. Osborne, M.L. Pantoya, *Combust. Sci. Technol.* 179 (8) (2007) 1467–1480.
- [21] A.Y. Dolgovorodov, M.N. Makhov, I.V. Kolbaney, A.N. Streletskii, V.E. Fortov, *JETP Lett.* 81 (7) (2005) 311–314.
- [22] K. Park, D. Lee, A. Rai, D. Mukherjee, M. Zachariah, *J. Phys. Chem. B* 109 (2005) 7290–7294.
- [23] A. Rai, K. Park, L. Zhou, M. Zachariah, *Combust. Theory Model.* 10 (2006) 843–848.
- [24] V.I. Levitas, M.L. Pantoya, B. Dikici, *Appl. Phys. Lett.* 92 (2008) 011921.
- [25] V.E. Sanders, B.W. Asay, T.J. Foley, B.C. Tappan, A.N. Pacheco, S.F. Son, *J. Propul. Power* 23 (4) (2007) 707–714.
- [26] M.L. Pantoya, V.I. Levitas, J.J. Granier, J.B. Henderson, *J. Propul. Power* (January 2008), submitted for publication.
- [27] M.A. Trunov, M. Schoenitz, E.L. Dreizin, *Combust. Theory Model.* 10 (4) (2006) 603–623.
- [28] M.A. Trunov, S.M. Umbrajkar, M. Schoenitz, J.T. Mang, E.L. Dreizin, *J. Phys. Chem. B* 110 (2006) 13094–13099.
- [29] A.G. Merzhanov, Y.M. Grigorjev, Y.A. Gal'chenko, *Combust. Flame* 29 (1) (1977).
- [30] V.I. Levitas, *Int. J. Solids Struct.* 35 (9–10) (1998) 889–940.
- [31] V.I. Levitas, *Int. J. Plasticity* 16 (7–8) (2000) 805–892.
- [32] T. Bazyn, H. Krier, N. Glumac, *Combust. Flame* 145 (4) (2006) 703–713.
- [33] T. Bazyn, H. Krier, N. Glumac, *Proc. Combust. Inst.* 31 (2007) 2021–2028.
- [34] V.I. Levitas, M.L. Pantoya, K.W. Watson, *Appl. Phys. Lett.* 92 (2008) 201917.